

**Mapping molecular potentials using pump-probe spectroscopy of vibrational wave packets' revival**Svyatoslav N. Blinov <sup>1</sup>, Victor V. Kimberg <sup>1,\*</sup>, Pavel O. Krasnov <sup>1</sup>, Faris Kh. Gelmukhanov,<sup>1,2</sup> and Sergey P. Polyutov <sup>1</sup><sup>1</sup>*International Research Center of Spectroscopy and Quantum Chemistry - IRC SQC, Siberian Federal University, 660041 Krasnoyarsk, Russia*<sup>2</sup>*KTH Royal Institute of Technology, Division of Theoretical chemistry and biology, SE-10691 Stockholm, Sweden*

(Received 28 February 2023; revised 22 May 2023; accepted 21 June 2023; published 11 July 2023)

In this study, we investigate the nuclear dynamics in nitrogen monoxide after valence ionization by a pump pulse and subsequent probing with a time-delayed x-ray pulse. We calculate the development of the resulting vibrational wave packet, taking into account three different ionization mechanisms: one-photon, multiphoton, and tunneling ionization. Using a two-time propagation method, we solve the nonstationary nuclear Schrödinger equation to obtain time-resolved x-ray absorption spectra (TRXAS), considering the finite duration of the probe pulse. Our simulations show that the TRXAS profile accurately reflects the vibrational wave packets' trajectory in the cationic ground state. Additionally, we find that the TRXAS evolution is highly sensitive to small changes in the probed potential energy curve, making it a useful tool for reconstructing molecular potentials and determining anharmonicity and equilibrium bond length. This method can be applied to other polyatomic molecules and pump mechanisms.

DOI: [10.1103/PhysRevA.108.013104](https://doi.org/10.1103/PhysRevA.108.013104)**I. INTRODUCTION**

Ultrafast pump-probe spectroscopy has a long-term history since the first invention of the lasers in the optical range. This is an extremely useful tool to study the dynamics, where the first (pump) pulse is used to trigger an electronic or nuclear process while the second (probe) pulse arriving at a delay time tests the system response in the framework of absorption or photoemission spectroscopy, allowing one to trace evolution of a system in real time. Based on these ideas, the whole new realms on femtochemistry developed by Zewail [1] were awarded a Nobel Prize in 1999. Modern x-ray spectroscopy [2,3], promoted by the recent advances of x-ray free electron laser (XFEL) radiation facilities [4] and high-order harmonic generation (HHG) sources [5,6], opens a new chapter of ultrafast pump-probe techniques. The main advantage of using x rays is their high element and site selectivity due to high localization of the core-orbitals, allowing one to address an atomic center of interest in complex molecular systems.

Time-resolved x-ray spectroscopy for investigation of photoexcited molecular processes have recently gained significant focus [3,7]. Before the XFEL era, these experiments were limited to a temporal resolution of 100 ps, restricting the time-resolved studies to probing metastable states and preventing direct insight into the fundamental dynamics occurring on the femtosecond timescale, for example, near conical intersections. With the advent of XFEL and HHG facilities, the availability of wavelength-tunable ultrashort x-ray pulses as a part of various pump-probe techniques makes the direct imaging of nonadiabatic nuclear dynamics possible. The limited spectral resolution of stationary x-ray spectroscopy can be

overcome using the high time resolution in x-ray pump-probe measurements of vibrational and rotational dynamics in real time. This makes modern x-ray spectroscopy an important complementary tool for mapping the intra- and intermolecular potential energy surfaces [8–10] along with the conventional and nonlinear vibrational spectroscopy, such as multidimensional techniques based on visible, IR, THz, IR-Raman, etc. processes [11,12]. The technique that combines the IR-pump with x-ray probe processes has been developed theoretically nearly two decades ago [13–15] where strong phase sensitivity of the scheme was shown.

Here we present further development of the theoretical framework for simulations of the ionization-induced vibrational dynamics probed with short time-delayed x-ray pulses. We consider the NO molecule as a study case since it was carefully addressed in recent experimental [16] and theoretical [13,17] studies. First, the molecular ensemble is irradiated by a short pump pulse ionizing the valence electron from the highest-occupied molecular orbital (HOMO)  $2\pi$ . We consider various mechanisms of ionization: a one-photon process triggered by an ultraviolet (UV) pulse, infrared (IR) multiphoton ionization, and tunneling ionization in the case of strong IR radiation. All considered ionization regimes lead to the electronic ground state of the cation  $\text{NO}^+$ . Since the equilibrium internuclear distance of the cation differs sufficiently from one of the neutral molecule, the ionization triggers vibrational wave packet (VWP) dynamics in the cation, which is studied by time-resolved x-ray absorption spectroscopy (TRXAS) using short time-delayed x-ray pulses. The present pump-probe scheme explored here is theoretically based on a fully quantum-mechanical description of the VWP and correspondent TRXAS profile, utilizing the concept of forward and backward propagation time [13–15]. We investigate the effect of shape and duration of the x-ray probe pulse on the TRXAS

\*vkimberg@sfu-kras.ru

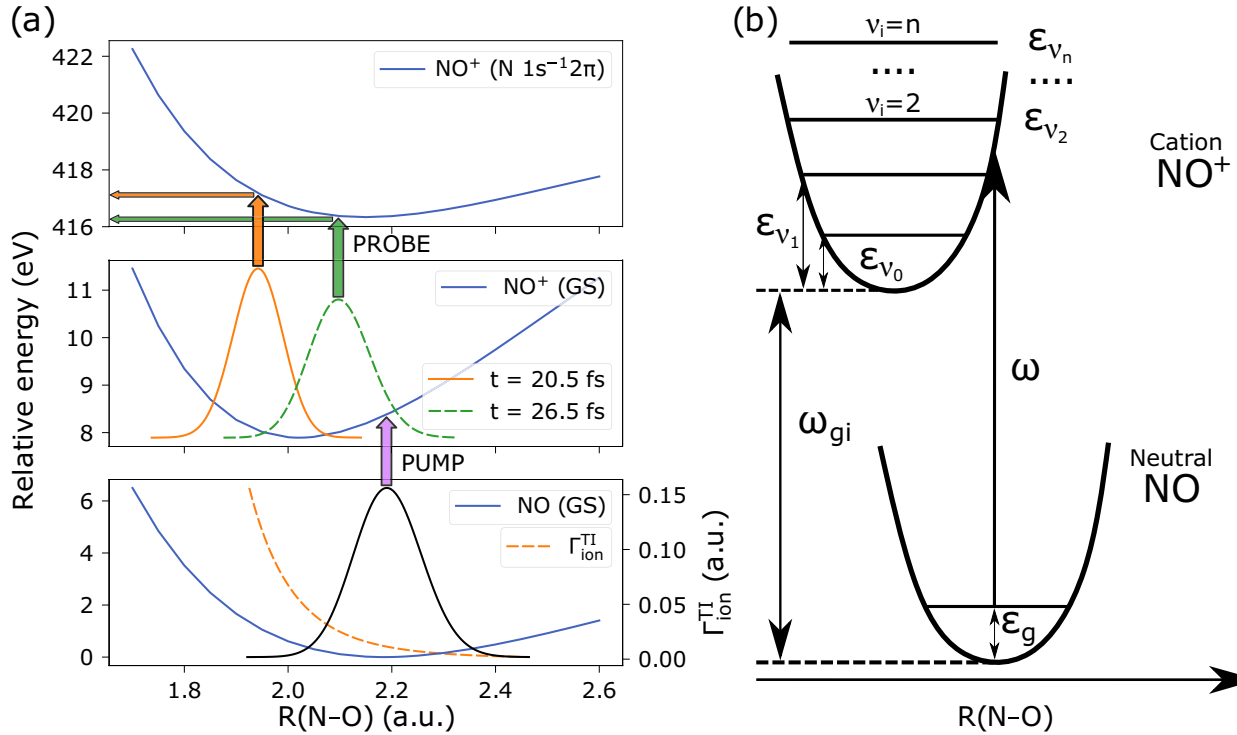


FIG. 1. (a) Scheme of the ionization-pump x-ray probe spectroscopy of NO molecule. *Ab initio* PECs (Sec. II A) and ionization rate  $\Gamma_{\text{ion}}^{\text{TI}}(R)$  computed using ADK theory (Sec. II B) are shown, the snapshots of the VWP  $|\varphi(t, R)|^2$  for the TI regime are obtained from numerical simulations (Sec. II D). (b) Vibrational excitation of the  $\text{NO}^+$  upon ionization (see text).

profile and show clearly that the VWP trajectory is accurately reflected in TRXAS, which makes this technique a very useful tool for extracting parameters of molecular potential energy curves with a reasonable accuracy.

The paper is organized as follows: Our theoretical approach is presented in Sec. II, where *ab initio* calculations (Sec. II A), photoionization mechanisms (Sec. II B), and time-dependent VWP and TRXAS simulation (Sec. II D) are described. The results are summarized in Sec. III, where we compare the VWP trajectory and the TRXAS profile (Sec. III A) for various probe pulse parameters (Sec. III B) and discuss the advantages for the potential mapping with the help of the TRXAS technique (Sec. III C). Our findings are summarized in Sec. IV. Atomic units are used through the paper unless otherwise stated.

## II. THEORETICAL APPROACH

Here we consider a two-step process: (i) valence ionization of the NO molecule by an IR or UV pulse followed by (ii) TRXAS measurements at the nitrogen *K*-edge, which probes the induced nuclear dynamics in the  $\text{NO}^+$  cation [Fig. 1(a)]. We assume ionization of the HOMO  $2\pi$  of NO. In our theoretical model the pump and probe pulses are not overlapped in time; we consider weak x-ray radiation in order to avoid nonlinear interaction effects, which corresponds to a recent experimental study using a HHG source [16]. Our approach is based on the Born-Oppenheimer approximation, decoupling the electronic and nuclear degrees of freedom. In this framework we first compute the potential energy curve

(PEC) for the ground neutral *g*, ground cationic *i*, and core-excited cationic *c* electronic states involved in the studied process. Modeling the nuclear dynamics is done with the help of solutions of the Schrödinger equation with the nuclear Hamiltonian

$$h_j = -\frac{1}{2\mu} \frac{d^2}{d^2R} + U_j(R), \quad j = g, i, c, \quad (1)$$

where  $\mu = 13\,611.7$  a.u. is the reduced mass of the NO and  $\text{NO}^+$  and  $U_j(R)$  is the PEC of the correspondent electronic state (see Fig. 1). The forward and backward propagation time concept is used for simulation of the TRXAS spectra.

Here we focus on a single core-hole state in the TRXAS spectra, as other core-ionized states in NO show well-separated absorption bands [16]. Without loss of generality all our conclusions can be applied to any number of nonoverlapped core-excited states. This shows yet another important aspect of the discussed pump-probe techniques: mapping of the PEC gradient of the core-ionized states. Indeed, the amplitude of the TRXAS oscillations is directly proportional to the gradient of the core-excited potential [see Fig. 1(a)], so a comparison of TRXAS trajectories for several core-excited cationic states in one experiment becomes a unique tool to obtain the relative gradients of those states.

### A. *Ab initio* calculations of the electronic structure and transitions

PECs of the electronic ground states of the neutral and ionized molecule and core-excited  $N\,1s \rightarrow 2\pi$  state of the

cation were computed using the CASSCF method implemented in ORCA software [18,19]. Scalar relativistic effects were included in the calculations using the second-order Douglas-Kroll-Hess (DKH2) Hamiltonian and appropriate atomic orbitals basis set cc-pVTZ-DK [20]. The computation time was sufficiently reduced with the help of the RI approximation [21–26]. The ground state PEC of NO molecule at every point was calculated in the framework of the CAS(7,6) approach, when seven valence electrons, four corresponding occupied, and two lowest unoccupied orbitals (total of six orbitals) were chosen as an active space. NO<sup>+</sup> cation contains one electron less; therefore, the active space size was CAS(6,6), which means that the same set of orbitals was considered. However, as we need a core-excited state also, this active space was used to optimize the valence orbitals. Next, these orbitals were considered initial ones without further optimization for CAS(8,7) case, where active space has been extended by adding N 1s orbital into it. The PECs are shown in Fig. 1(a) along with schematic electronic transition for valence ionization (pump) and core-excitation of an ion (probe). The used method was checked for convergence using the variation of the basis set and the size of the active space. The vibrational frequency and anharmonicity of the ground (1887.79 and 14.61 cm<sup>-1</sup>, respectively) and ionic (2361.77 and 16.02 cm<sup>-1</sup>, respectively) states are in a good agreement with those known from the literature (1904.204 and 14.075 cm<sup>-1</sup> for the ground state [27] and 2376.42 and 16.262 cm<sup>-1</sup> for the ionic [28] state), which confirms accuracy of the *ab initio* PECs. We also computed the transition dipole moment from the ionic ground to the core-excited state, which shows very weak dependence on the internuclear distance and thus has no sufficient effect on the TRXAS profiles.

### B. Photoionization-induced nuclear dynamics

When a molecule absorbs a photon of energy higher than the binding energy of HOMO electron (e.g., UV or x-ray photon) one-photon ionization (OPI) occurs, also known as linear photoionization since the ionization rate in this case is proportional to the incoming light intensity. In the case when photon energy is smaller than the electron binding energy (e.g., IR photon), ionization may occur within the multiphoton ionization (MPI) process. When the intensity of IR light becomes rather high the process of tunneling ionization (TI) becomes dominant. The distinction between MPI and TI can be done with the help of well known Keldysh parameter [29]  $\gamma = \kappa \omega / E_{\text{IR}}$ , where  $\kappa = \sqrt{2I_p}$ ,  $I_p$  is ionization potential,  $\omega$  is photon frequency, and  $E_{\text{IR}}$  is the electric-field strength. When  $\gamma \gg 1$  the MPI predominantly happens, and TI regime dominates when  $\gamma \ll 1$ . For example, for experimental parameters of the recent NO study by Saito *et al.* [16] ( $\omega = 1.6 \mu\text{m} = 0.028 \text{ a.u.}$ ,  $I \approx 10^{14} \text{ W/cm}^2$ ,  $E_{\text{IR}} = 0.053 \text{ a.u.}$ ,  $I_p = 9.26 \text{ eV}$ ) estimation gives  $\gamma \approx 0.5$  providing the TI regime. The photoionization process may affect sufficiently vibrational and rotational excitation of a molecule.

In the present study we consider a fixed-in-space molecule, more precisely we neglect the rotational degrees of freedom, in order to avoid complexity and to focus on the time-dependent XAS manifestation itself, while the effects of rotational degrees of freedom and rotational wave packets'

excitation discussed in detail elsewhere [30]. However, molecular rotation deserves a short comment here. Interaction of the molecular ensemble with a strong short IR pulse results in formation of a coherent rotational wave packet with a typical rotational revival period of several picoseconds, e.g., 4 ps for N<sub>2</sub> and CO molecules [31,32]. The fact that vibration revival time (about 1 ps) is considerably shorter than the rotational revival provides a possibility to perform TRXAS measurement of vibrational revival within one period of the rotational revival. In this case, all general characteristics of TRXAS discussed below will be present in measurements with the delay times shorter than the rotational revival time.

### C. OPI, MPI, and TI regimes

Let us now discuss vibrational excitation for the three ionization regimes (OPI, MPI, and TI) mentioned above. At weak and moderate laser intensity, both OPI and MPI can be described in the framework of the lowest-order perturbation (LOP) theory of the electron-field interaction [33], which is valid while the electric-field strength is small as compared with atomic electric field. In this case, the “sudden transition” approximation can be applied, implying that the vibrational excitation of the molecular ion will follow the Franck-Condon (FC) distribution obtained as an integral overlap between the initial and final states vibrational wave functions. A commonly used model for simulation of the TI rate is the so-called Ammosov-Delone-Krainov (ADK) model [34], which was developed for the case of a hydrogen-like atom in a static electric field, with modifications introduced for the real many-electron atoms. This model was further developed for description of tunneling ionization in molecules [16,35]. Recently, the more advanced weak-field asymptotic theory of tunneling ionization was developed [36], generalizing the earlier theory from spherically symmetric atomic potentials to molecular potentials without any symmetry [37,38]. All mentioned models consider atomic or molecular interaction with the static electric field. Both theory and experiment in molecules [39,40] shows that TI may result in sufficient deviation of the FC vibrational excitation distribution, because of strong  $R$  dependence of the ionization probability in high laser fields. It is worthwhile noting that, with further increase of the field, the TI transforms to the so-called over barrier ionization: the laser intensity is high enough to deform the electrostatic potential so much that an electron is no longer bound and can pass over the top of the barrier without tunneling. At such high intensities, the ADK theory does not work very well. The discrepancy of molecular potential ADK theory starts at laser intensities higher than  $I > 10^{15} \text{ W/cm}^2$ , as it was shown for a number of diatomics [35]. In the present paper we use IR intensity below this limit.

The VWP  $\varphi(t, R)$  in cation triggered by photoionization can be written as

$$\varphi(t, R) = \sum_{v_i=0}^n a_{v_i}(t) \psi_{v_i}(R) e^{-i\epsilon_{v_i} t}, \quad (2)$$

where  $a_{v_i}(t)$ ,  $\psi_{v_i}(R)$ , and  $\epsilon_{v_i}$  are the amplitude, stationary eigenfunctions and the eigenenergies of the vibrational state  $v_i$  of the ion [see Fig. 1(b)]. The sum is taken over a number of vibrational states showing a sufficient population on

the transition from the neutral ground state. The vibrational amplitudes are governed by the following equations for the closed quantum system [31,32]:

$$\frac{da_{v_i}}{dt} = -ia_g(t) \langle \psi_{v_i} | V_{ig}(t, R) | \psi_g \rangle e^{i(\epsilon_{v_i} - \Omega_p)t},$$

$$\Omega_p = N\omega - (\epsilon_{\mathbf{k}} + I_p - \epsilon_0),$$

where  $\epsilon_{\mathbf{k}}$  is the energy of the photoelectron with the momentum  $\mathbf{k}$ ,  $\psi_g$ , and  $\epsilon_0$  are the lowest vibrational wave function and energy of the ground state,  $a_g(t)$  its amplitude, and  $V_{ig}(t, R)$  is the operator of the  $N$ -photon ionization by the pump field with the frequency  $\omega$ . We assume a reasonable approximation that the ionization rate of the neutral system is weak and suppose  $a_g(t) \approx 1$ . In this case vibrational amplitudes of the ionized state read

$$a_{v_i}(t) = -i \int_{-\infty}^t \langle \psi_{v_i} | V_{ig}(t_1, R) | \psi_g \rangle e^{i(\epsilon_{v_i} - \Omega_p)t_1} dt_1. \quad (3)$$

Moreover, in our model we consider the situation when the delay time of the probe pulse is much longer than the duration of the pump pulse  $\tau_p$  (half width at half maximum, HWHM). This means that at time  $t \gg \tau_p$ , when the system interacts with the probe field, the amplitude  $a_{v_i}(t) = a_{v_i}(\infty)$  is time-independent:

$$a_{v_i}(\infty) = -i \int_{-\infty}^{\infty} \langle \psi_{v_i} | V_{ig}(t_1, R) | \psi_g \rangle e^{i(\epsilon_{v_i} - \Omega_p)t_1} dt_1,$$

$$\varphi(t, R) = \sum_{v_i=0}^n a_{v_i}(\infty) \psi_{v_i}(R) e^{-i\epsilon_{v_i}t}. \quad (4)$$

Let us consider the Gaussian shape of the pump pulse amplitude with maximum at  $t = t_p$

$$P(t) = A \exp \left[ -\left( \frac{t - t_p}{\tau_p} \right)^2 \ln 2 \right], \quad (5)$$

where  $A = 1/(\tau_p \sqrt{2\pi/\ln 2})$ . In this case,  $V_{ig}(t, R) = V_{ig}(R)P(t)$  and the VWP (2) can be written as

$$\varphi(t, R) = e^{-i\Omega_p t_p} \sum_{v_i} e^{-i\epsilon_{v_i}(t-t_p)} \psi_{v_i}(R) \langle \psi_{v_i} | V_{ig}(R) | \psi_g \rangle$$

$$\times \exp \left( -(\epsilon_{v_i} - \Omega_p)^2 \tau_p^2 \frac{\ln 2}{8} \right). \quad (6)$$

Below we put the origin of the pump pulse at time zero ( $t_p = 0$ ) and neglect the dynamics of the vibrational wave packet within the pump pulse. It is a reasonable assumption which is valid for the pump pulse considerably shorter than the vibration period (14 fs for NO) and it is satisfied for a few fs pulse when  $\epsilon_{v_i} \tau_p \ll 1$ . Within this ‘‘sudden transition’’ approximation ( $\tau_p \rightarrow 0$ ) the nuclear wave packet (6) is simply the solution of the Schrödinger equation

$$\varphi(t, R) = e^{-iHt} V_{ig}(R) \psi_g(R), \quad (7)$$

with initial condition  $\varphi(t = 0, R) = V_{ig}(R) \psi_g(R)$ .

Let us now specify the ionization rates and corresponding amplitudes for the different ionization regimes. In the case of weak interaction, when the LOP theory is applicable (OPI and MPI) the ionization rates for one- and  $N$ -photon ionization

processes:

$$\Gamma_{\text{ion}}^{\text{OPI}}(t) = |E_{UV} d_{gi}|^2 = \sigma_{\text{ion}}^{\text{OPI}} I / \hbar \omega,$$

$$\Gamma_{\text{ion}}^{\text{MPI}}(t) = |(E_{\text{IR}} d_1)(E_{\text{IR}} d_2) \cdots (E_{\text{IR}} d_N)|^2$$

$$= \sigma_{\text{ion}}^{\text{MPI}} (I / \hbar \omega)^N$$

are usually rather low. Here  $I = I(t)$  is the intensity of the pump radiation. Moreover, here we neglect rather weak  $R$  dependence of the transition dipole moments  $d_{gi}$ ,  $d_i$  ( $i = 1, \dots, N$ ) near the equilibrium geometry where the initial vibrational wave function  $\psi_g$  is localized. In this case the amplitudes of ionization can be found as  $V_{ig}^{\text{LOP}}(0, R_0) = [\Gamma_{\text{ion}}^{\text{OPI/MPI}}(0)]^{1/2}$  and

$$\langle \psi_{v_i} | V_{ig}^{\text{LOP}} | \psi_g \rangle \approx V_{ig}^{\text{LOP}} \langle \psi_{v_i} | \psi_g \rangle. \quad (8)$$

In the case of TI by a short (few-cycle) intense IR pulse, the time-dependence of the ion population show a step-like behavior, as ionization happens at the local maxima of the electric field [41,42]. The so-called ground-state polarization effect leading to recapturing of the ionized electron due to increased Coulomb potential may lead to the time-oscillation in the ion population during the interaction with the laser pulse, as it was observed in Xe atoms [42] and NO molecules [16]. This effect however does not play any role in our study since we probe the induced dynamics after the IR pulse left the system (nonoverlapped pump and probe pulses) and thus neglected. However, the  $R$  dependence of the ionization rate cannot be neglected in the case of strong-field interaction. Our estimations for TI rate  $\Gamma_{\text{ion}}^{\text{TI}}(E_{\text{IR}}, R)$  for the fixed-in-space molecule with molecular axis along the electric-field polarization was performed using ADK equation [34,35,41]

$$\Gamma_{\text{ion}}^{\text{TI}}(E_{\text{IR}}, R) = \sqrt{\frac{3E_{\text{IR}}}{\pi \kappa^3}} \frac{B(m)^2}{2^{|m|} |m|! \kappa^{2/\kappa - 1}} \left( \frac{2\kappa^3}{E_{\text{IR}}} \right)^{2/\kappa - |m| - 1}$$

$$\times \exp[-2\kappa^3 / (3E_{\text{IR}})],$$

$$B(m) = \sum_l C_l Q(l, m),$$

$$Q(l, m) = (-1)^m \sqrt{\frac{(2l+1)(l+|m|)!}{2(l-|m|)!}}, \quad (9)$$

with  $C_l$  being the parameters for the  $\pi$  orbital of NO taken from Ref. [35], and  $\kappa = \sqrt{2I_p}$ . The  $R$  dependence of  $\Gamma_{\text{ion}}^{\text{TI}}$  stems from  $R$  dependence of the molecular ionization potential  $I_p$ , found as a difference of the neutral and cationic ground-state energies; its  $R$  dependence is plotted in Fig. 1(a) for the field amplitude  $E_{\text{IR}} = 0.053$  a.u. ( $I = 10^{14}$  W/cm<sup>2</sup>) and  $m = 1$ . (See Appendix A and Fig. 13. for varied field intensity). We consider here the case of nonoverlapped pulses, when the delay time of the x-ray probe  $t_X$  is much longer than the duration of the pump pulse  $\tau$ . Then at the observation time  $t_X \gg \tau$  the amplitudes of the ionic states  $a_i(t_X)$  becomes time-independent [see Eqs. (3) and (4)] and proportional to the generalized FC amplitudes [39,43]

$$\langle \psi_{v_i} | V_{ig}^{\text{TI}} | \psi_g \rangle = \langle \psi_{v_i} | \sqrt{\Gamma_{\text{ion}}^{\text{TI}}(R)} | \psi_g \rangle, \quad (10)$$

while the total ionic population is  $\sum |a_i(t_X)|^2 = \int dt \Gamma_{\text{ion}}^{\text{TI}}$ . We assume that the ionic population does not exceed a few

percent of the initial molecular ensemble  $\sum |a_i|^2 \ll 1$  [41], ensuring that the VWP dynamics is not affected by the saturation effects. In the present study we do not pay attention to absolute value of the ionization, but focus on the dynamics of the induced VWP (2), (7). The wave packet  $\varphi(t, R)$  allows us to find the trajectory of the VWP center of gravity  $\langle R \rangle$ :

$$\langle R(t) \rangle = \langle \varphi(t, R) | R | \varphi(t, R) \rangle. \quad (11)$$

To summarize this section, the VWP formed by MPI is equivalent to that formed via OPI within the sudden transition approximation and can be described by Eqs. (2) and (7) with ionization amplitudes (8). For the case of TI the  $R$  dependence of the ionization must be taken into account, due to sufficient disturbance of the molecule geometry in the strong ionizing field, thus the induced VWP is computed using ionization amplitudes (10). The VWP trajectory is computed according to Eq. (11). It is also worthwhile to note, that typical IR frequency used in TI and MPI experiments (e.g., 1.6  $\mu\text{m}$  [16]) is far away from resonant vibrational transitions in NO and  $\text{NO}^+$  and thus VWP dynamics is not affected by direct IR excitation and IR-Raman process.

#### D. Time-resolved probe x-ray absorption spectra

Let us now consider probe signal–time-dependent absorption of a weak probe x-ray pulse of frequency  $\omega_X$  resonant to the transition between cation ground and N  $1s \rightarrow 2\pi$  core-excited states [Fig. 1(a)] that arrives at the delay time  $t_X$  after the pump pulse

$$\begin{aligned} \mathcal{E}_X &= \mathbf{e}_X E_X^0 \Delta_X(t) e^{-i\omega_X t}, \\ \Delta_X(t) &= e^{-\ln \sqrt{2} |(t-t_X)/\tau_X|^{2k}}, \end{aligned} \quad (12)$$

here  $\tau_X$  is the half width at half maximum (HWHM) of the intensity temporal envelope  $I_X \propto |\mathcal{E}_X|^2$ ,  $\mathbf{e}_X$  and  $E_X^0$  are the polarization unit vector and maximum strength of the electric field, respectively. Here we describe the envelope of the probe pulse  $\Delta_X(t)$  using generalized Gaussian profile defined by parameter  $k$ :  $k = 1$  corresponds to a Gaussian Fourier transform-limited pulse, while  $k \gg 1$  corresponds to the pulse envelope of rectangular shape. In our study we compare Gaussian ( $k = 1$ ) and quasirectangular ( $k = 3$ ) pulse envelopes.

X-ray probe pulse promotes the N  $1s$  electron of  $\text{NO}^+$  to the  $2\pi$  orbital, creating, along with the electronic excitation, the core-excited vibrational packet,  $|\Phi(t)\rangle$  [13,14]

$$|\Phi(t)\rangle = e^{ih_c t} \zeta |\varphi(t)\rangle, \quad (13)$$

where  $h_c$  is the nuclear Hamiltonian (1) of the core-excited electronic state and  $\zeta = (\mathbf{d}_{ic} \cdot \mathbf{e}_X)$ ,  $\mathbf{d}_{ic}$  is the electronic transition dipole moment between the ground and core-excited N  $1s \rightarrow 2\pi$  states of  $\text{NO}^+$ . Within the framework of nonoverlapped pump and probe pulses and in approximation of the weak x-ray field the probe absorption spectrum (TRXAS profile) reads [13]

$$\begin{aligned} P(\Omega, t_X) &= \int_{-\infty}^{\infty} d\epsilon P_0(\Omega - \epsilon, t_X) \Delta(\epsilon, \Gamma_c), \\ P_0(\Omega, t_X) &= \langle \Phi(\Omega, t_X) | \Phi(\Omega, t_X) \rangle, \end{aligned} \quad (14)$$

where

$$|\Phi(\Omega, t_X)\rangle = \int_{-\infty}^{+\infty} dt \Delta_X(t) |\Phi(t)\rangle e^{-i\Omega t}, \quad (15)$$

and  $\Delta(\epsilon, \Gamma_c) = \Gamma_c / (\pi[\epsilon^2 + \Gamma_c^2])$  is the normalized Lorentzian,  $\Gamma_c = 0.06 \text{ eV}$  [44] (HWHM) is the lifetime broadening of the core-excited state,  $\Omega = \omega_X - \omega_{ic}$ ,  $\omega_{ic}$  is the difference between minima of the ionic core-excited and ionic ground states PECs. According to our numerical simulations the difference between  $P(\Omega, t_X)$  and  $P_0(\Omega, t_X)$  is negligibly small for  $\Gamma_c = 0.06 \text{ eV}$ . To compute  $|\Phi(t)\rangle$  we apply the concept of forward-backward time-propagation following Refs. [13,15,45,46], where the wave packet in the core-excite state is computed as  $|\Phi(t)\rangle = \lim_{t_1 \rightarrow 0} |\Phi(t_1, t)\rangle$  using auxiliary two-time wave packet  $\Phi(t_1, t)$ . In this method the VWP  $|\varphi(t)\rangle$  evolves from time 0 up to  $t$  with the nuclear Hamiltonian of the ionic state  $h_i$ . The x-ray field promotes  $|\varphi(t)\rangle$  to the core-excited state at the moment  $t$ . To find  $\Phi(t_1, t)$  we solve Schrödinger equation

$$i \frac{\partial |\Phi(t_1, t)\rangle}{\partial t_1} = h_c |\Phi(t_1, t)\rangle, \quad (16)$$

with initial condition  $|\Phi(t, t)\rangle = \zeta |\varphi(t)\rangle$  in the inverse direction of time from moment  $t_1 = t$  up to  $t_1 = 0$  in the core-excited potential energy surface.

Equations (13) and (15) allow us to understand the dependence of the TRXAS profile (14) on the duration of the x-ray probe pulse. When the probe pulse duration tends to zero  $\Delta_X(t) \propto \delta(t - t_X)$ , where  $\delta$  is the Dirac  $\delta$  function, Eq. (15) provides that

$$|\Phi(\Omega, t_X)\rangle \propto \zeta e^{ih_c t_X} e^{-ih_i t_X} V_{ig}(R) |\psi_g(R)\rangle,$$

and the TRXAS profile (14) reads

$$P_0(\Omega, t_X) = \langle \psi_g | V_{ig}^* e^{ih_i t_X} |\zeta|^2 e^{-ih_i t_X} V_{ig} | \psi_g \rangle. \quad (17)$$

The above equation shows an important result: the probe signal does not depend on the delay time  $t_X$  when the pump and probe pulses are ultrashort and the transition dipole moment of x-ray absorption ( $\zeta \propto d_{ic}$ ) is  $R$  independent  $P_0(\Omega, t_X) \propto |\zeta|^2 |\langle \psi_g | V_{ig}^* | \psi_g \rangle|$ . This observation is in full agreement with our previous studies [31,32] and is nicely confirmed in the present numerical simulations, showing a decrease of the amplitude of temporal TRXAS modulations with the shortening of the x-ray pulse.

We compute also the trajectory of the center of gravity of TRXAS spectra  $\langle \Omega \rangle$  [17]

$$\langle \Omega(t_X) \rangle = \frac{\int \Omega P(\Omega, t_X) d\Omega}{\int P(\Omega, t_X) d\Omega}. \quad (18)$$

### III. RESULTS AND DISCUSSIONS

Using theoretical model described above we performed numerical simulations for  $\text{NO}^+$  ground state VWP dynamics and correspondent TRXAS profiles. We study the sensitivity of the TRXAS spectroscopy varying parameters of x-ray pulse and the accuracy of the molecular potentials. We compare VWP dynamics induced by OPI and MPI described in LOP theory with one triggered by TI. In all simulations we supposed that

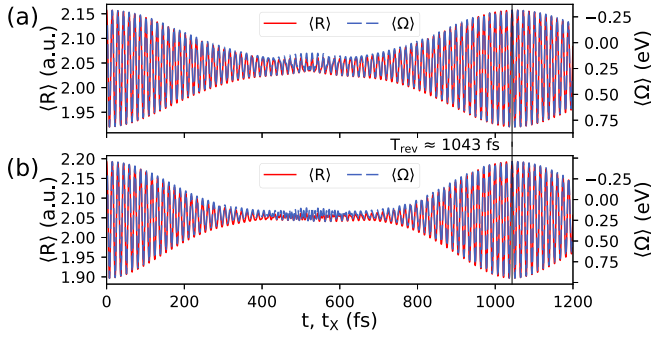


FIG. 2. Trajectory of the  $\text{NO}^+$  ground state VWP  $\langle R \rangle$  (11) (red solid line) vs TRXAS center of gravity  $\langle \Omega \rangle$  (18) (blue dashed line) as functions of time for (a) TI and (b) OPI and MPI cases;  $\tau_x = 0.2$  fs,  $k = 1$ .

the ionization rate is small enough to avoid any saturation effects; nonoverlapped pump and probe pulses are considered.

### A. Vibrational wave packet trajectory observed by TRXAS

Let us first discuss the dynamics of the cation ground state VWP induced by ionization of the neutral molecule and how it is reflected in the TRXAS profile. The trajectory of the ionic ground state VWP trajectory  $\langle R \rangle$  is shown in Fig. 2 with red lines computed for TI [Fig. 2(a)] and LOP [Fig. 2(b)] theory. In the both cases, the trajectory profile shows the similar main features. First, the high-frequency oscillation period ( $T \approx 14$  fs) corresponds to the harmonic vibrational frequency of the ionic ground state  $\omega_e = 2361.77 \text{ cm}^{-1}$ . At the moment of ionization the VWP is highly localized near the vertical transition point. The ionic PEC is shifted significantly towards the shorter bond length [see Fig. 1(a)] which results in high amplitude oscillations of the induced VWP up to  $\approx 200$  fs. Then, the VWP experiences delocalization, manifesting in sufficient reduction of the oscillation amplitude in the time-range  $\approx [400, \dots, 650]$  fs. This time-range corresponds to a half of the so-called revival time — the time when VWP return to the high degree of localization (see  $t_x = T_{\text{rev}} \approx 1043$  fs, Fig. 2) and its dynamics restarted. The revival period  $T_{\text{rev}}$  can be used for high-accuracy determination of the anharmonicity  $x_e \omega_e$  of the PEC, as discussed below (Sec. III C).

The VWP induced by the TI (Fig. 2(a)) and OPI and MPI (Fig. 2(b)) show quite similar trajectories with exactly the same values of  $T$  and  $T_{\text{rev}}$ . This can be easily understood from the fact that the PEC parameters  $\omega_e$  and  $x_e \omega_e$  are the same in the field-free case, i.e., when the pump pulse already left the system. The regime of the photoionization, however, may affect the initial vibrational populations of the ionic states: in the case of TI the lower vibrational states are more populated, as compared with the case of LOP theory (see discussion in Sec. III C). Due to this, the delocalization phenomenon is slightly weaker in the TI case. Similar effect was observed experimentally in the TI of  $\text{H}_2$  [39].

Figure 2 shows that the trajectory of TRXAS center of gravity (blue dashed lines) follows very well the VWP trajectory (red solid lines). This observation confirms applicability of TRXAS for mapping of the ultrafast VWP dynamics. The mechanism of the mapping can be understood considering the

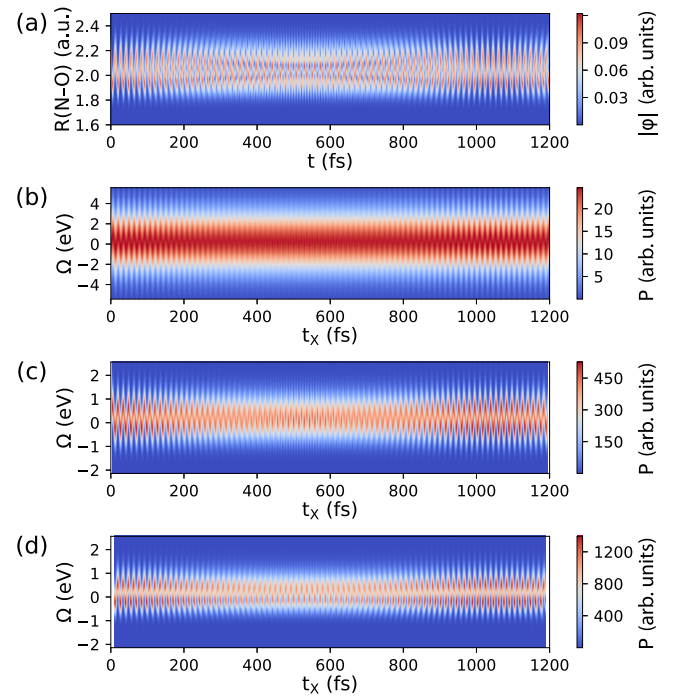


FIG. 3. Time and  $R$  dependence of the modulus of the VWP  $|\varphi(t, R)|$  for (a) the TI regime (7), (10); time and energy dependence of TRXAS for the probe x-ray pulse duration (b)  $\tau_x = 0.2$ , (c) 1.0, and (d) 2.0 fs,  $k = 1$ .

so-called reflection principle [10,47–49], illustrated schematically in Fig. 1(a). Due to a sufficient shift of the core-excited  $\text{N } 1s^{-1}2\pi$  state PEC, vertical transition for the VWP snapshots at 20.5 and 26.5 fs results in a clear distinction in the energy domain [see the solid orange and dashed green profiles in the middle panel of Fig. 1(a)]. A minor discrepancy between the VWP trajectory and TRXAS appears at the delocalization time-region and it is higher for OPI and MPI as compared with TI, as degree of delocalization is higher in the OPI and MPI case. The TRXAS profile is rather sensitive to the duration and shape of x-ray probe pulse, so that the balance between temporal and energy resolution has to be found.

### B. TRXAS dependence on the probe pulse shape

A fully temporal coherent laser pulse has a constant phase across all frequency harmonics, which making up the pulse. That type of pulse, also known as Fourier-transform-limited (FTL) pulse, has the minimum possible duration for a given spectral bandwidth, which is defined by time-bandwidth product. For FTL pulse of Gaussian shape, used in our simulations, the product of pulse duration and bandwidth is  $\tau_x(\text{FWHM, fs})\Delta\omega_x(\text{FWHM, eV}) \approx 0.456$ . For  $\tau_x = 0.2$  fs pulse, discussed in the previous section, the broad spectral bandwidth of  $\Delta\omega_x = 2.28 \text{ eV}$  creates sufficient uncertainty in the energy domain. The effect of the probe pulse duration is clearly illustrated in the two-dimensional (2D) maps of Fig. 3, where  $(t, R)$  dependence of the VWP [Fig. 3(a)] is compared against  $(t_x, \Omega)$  dependence of TRXAS spectra for  $\tau_x = 0.2$  fs [Fig. 3(b)], 1.0 fs [Fig. 3(c)], and 2.0 fs [Fig. 3(d)].

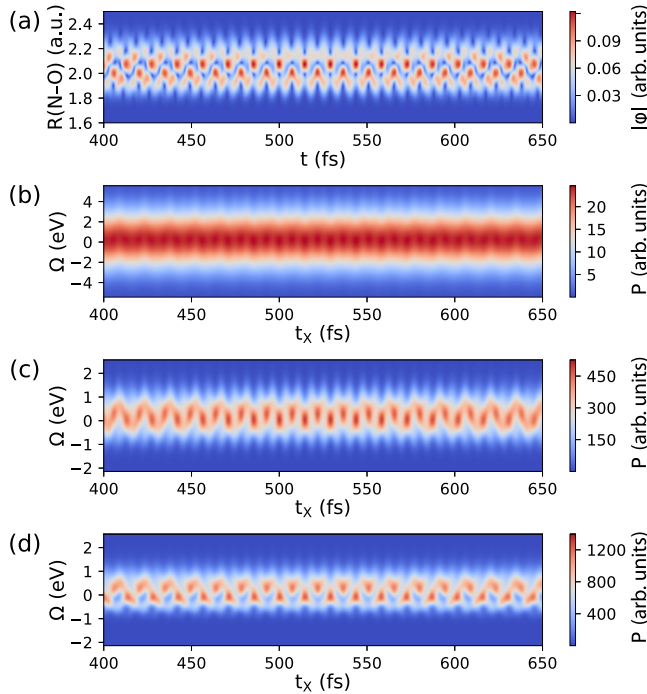


FIG. 4. Same as Fig. 3, but with zoom on the VWP delocalization time interval [400, . . . , 650] fs.

Apparently, much sharper mapping of the VWP by TRXAS is observed for the longer pulse duration, which is most important is the delocalization region [400, . . . , 650] fs, as presented in more details in Fig. 4. It is worthwhile noting that the amplitude of the TRXAS modulations decrease drastically with decreasing the probe pulse duration in full agreement with our theoretical analysis of Eq. (17) and previous studies [31,32]. Indeed, the TRXAS amplitude decreases 2.65 times when x-ray pulse is shortened twice (2 to 1 fs), and 56.6 times when pulse duration decreases ten times from 2 to 0.2 fs [see side color boxes for Figs. 3(b)–3(d) and 4(b)–4(d)]. Moreover, the two-dimensional (2D) map looks much more blurred in the case of  $\tau_x = 0.2$  fs pulse, making the extraction of the full  $(t, R)$  dependence of the VWP rather difficult, while for 2.0 fs pulse the maxima positions of the VWP are well recognizable in the TRXAS map. The reason for this is that both high temporal and high spectral resolution are required in this case, due to fast temporal beatings of the wave packet. For the OPI and MPI regimes the VWP dynamics is rather similar (with some exception in the delocalization region) and thus omitted here. As one can see, the vibrational dynamics of NO is on the order of femtoseconds, and 1–2 fs pulses are well suitable for recording the VWP. However, the example of 0.2 fs pulse deserves reader’s attention because sub-fs pulses become available from HHG sources and can be applied for studying the ultrafast VWP dynamics (e.g., nonadiabatic dynamics).

The trajectory of the TRXAS center of gravity (Fig. 2), however, reproduces well the trajectory of the VWP and does not depend drastically on the pulse duration. The TRXAS trajectories for pulse duration  $\tau_x = 0.2, 1.0,$  and 2.0 fs in the range of VWP delocalization show only minor

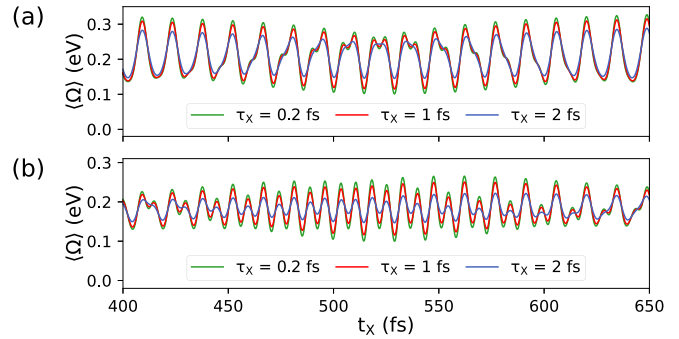


FIG. 5. Dependence of TRXAS center of gravity (18) on the pulse duration  $\tau_x = 0.2, 1.0,$  and 2.0 fs (HWHM) for (a) TI and (b) OPI and MPI (b) regimes. Gaussian pulse envelope,  $k = 1$  in (12).

differences (see Fig. 5). The effect of the probe pulse duration is stronger in the case of OPI and MPI as compared with TI, since the VWP experience higher degree of the delocalization. The results for a quasirectangular x-ray pulse shape [ $k = 3$  in (12)] with  $\tau_x = 0.2, 1.0,$  and 2.0 fs are summarized in Fig. 6. One can see, that the spectral profiles shows smaller differences with varying the pulse duration, as compared with the Gaussian-pulse case. This results from a generally broader spectral profile of the quasirectangular pulse, having numerous sidebands in the energy domain.

In a real experimental situation probe pulse may deviate from a Gaussian Fourier-transform-limited shape, resulting in a larger spectral and/or temporal broadening. Moreover, the soft x-ray pulses commonly available from the present day XFEL facilities are generated within self-amplified spontaneous emission (SASE) scheme and thus have rather limited spectral coherence ( $\Delta\omega_x/\omega_x \sim 1\%$  in the soft-x-ray range). The coherence may be sufficiently improved by using self-seeding XFEL schemes [50]. On the other hand, SASE radiation can also be adapted for high-resolution pump-probe measurements using stochastic covariance techniques [51]. HHG sources provide ultrashort sub-fs pulses, which are well suited for studying ultrafast dynamics with high-time resolution, yet having moderate spectral resolution. One needs to find a trade-off between temporal and spectral resolution for a particular study case. The main goal of the present study is to extract the PEC parameters and thus the probe pulse duration needs to be sufficiently smaller than the period of

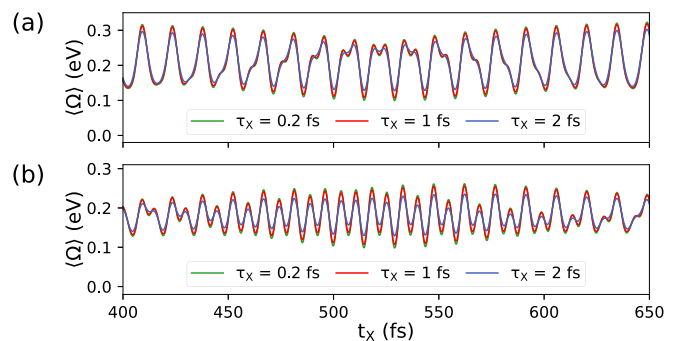


FIG. 6. Same as Fig. 5, but for quasirectangular pulse shape,  $k = 3$  in (12).

harmonic oscillations,  $T \approx 14$  fs, so  $\tau_X = 1$  fs pulse provides a reasonably good accuracy and is used in the following simulations.

### C. Characterizing potential energy curve parameters via TRXAS revivals

Knowledge of molecular PECs is important for predicting physical properties as well as the chemical dynamics of molecular systems. High-accuracy PECs for a stable (e.g., ground) states of diatomics can be extracted from experimental rovibrational spectra using well-known Rydberg-Klein-Rees (RKR) [52] method, which utilizes the observed variation of the vibrational energies and rotational constants with the vibrational quantum number. The potential curve is generated point-wise based on evaluation of the left and right classical turning points of the PEC. The main advantage of the RKR method is that it has no assumption on the PEC shape. However, the PEC of an isolated state can be well approximated with a Morse (Appendix B) or generalized Morse [53] PEC shape. In this case, the high-resolution measurement of the vibrational energies allows us to fit the harmonic frequency and anharmonicity of the PEC even for highly excited unstable states, while the equilibrium position of the excited electronic states can be found using the Frank-Condon analysis of the observed vibrational progression. For example, PEC parameters for highly excited unstable cationic electronic states far from equilibrium geometry was recently obtained using resonant Auger scattering (RAS) [9] with a very good agreement with *ab initio* simulations. Similarly, high-resolution resonant inelastic x-ray scattering (RIXS) [54,55] were applied to study excited neutral states.

In the present study we show that the TRXAS can be used for accurate determination of the anharmonicity and equilibrium internuclear distance of PECs, as well as for detecting a small PEC deviation far from equilibrium. The method is not limited to the ionic ground state, presented here as a study case, but can be extended for numerous valence and ionic excited states when another pump mechanism is applied.

PECs along the stretching mode of an isolated electronic state of diatomics can be approximated with rather high accuracy using the Morse potential shape (B1). The Morse fitting of *ab initio* PECs for the  $\text{NO}^+$  ground state results in following fundamental parameters:  $\omega_e = 2361.773\,27\text{ cm}^{-1}$ ,  $x_e\omega_e = 16.022\,79\text{ cm}^{-1}$ , and  $R_i = 2.021\text{ a.u.}$  In Fig. 7 we compare the original potential (solid red curve) with harmonic one ( $x_e\omega_e = 0$ , dash-dotted green curve) and one with doubled anharmonicity ( $x_e\omega_e \approx 32.05\text{ cm}^{-1}$ , dashed blue curve). Our simulations of TRXAS mapping the VWP dynamics in those three PECs are summarized in Fig. 8. First, let us pay attention to the VWP revivals reflected in the TRXAS profiles. Measurement of the revival time allows us to compute the anharmonicity as  $x_e\omega_e = \pi/T_{\text{rev}}$ . Obviously,  $T_{\text{rev}} = \infty$  for the harmonic potential. For the two anharmonic PEC (Fig. 7) we found  $T_{\text{rev}} \approx 1045\text{ fs}$  ( $\omega_e x_e \approx 16.02\text{ cm}^{-1}$ ) and  $523\text{ fs}$  ( $\omega_e x_e \approx 32.05\text{ cm}^{-1}$ ). Our numerical experiment shows that anharmonicity can be found from the vibrational revivals with reasonable accuracy. Indeed, we get  $x_e\omega_e \approx 16.1\text{ cm}^{-1}$  and  $32.4\text{ cm}^{-1}$  for the solid red and dashed blue PECs (see Fig. 7), respectively, using the above-mentioned revival times.

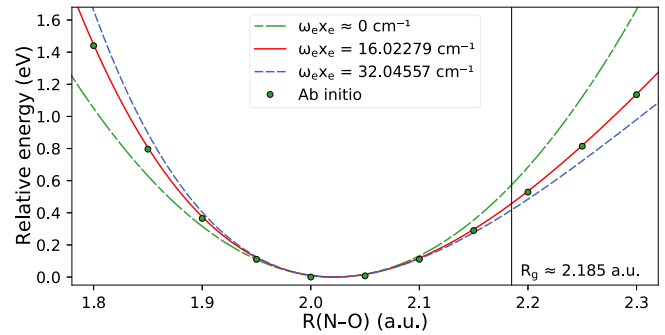


FIG. 7. PECs of ground state  $\text{NO}^+$ : *ab initio* (circles), fitted Morse (solid red line), harmonic (dash-dotted green line), and transformed Morse with doubled anharmonicity (dashed blue line). The equilibrium distance of the NO ground state is shown by the vertical line.

The fine oscillation of the TRXAS profile clearly show different vibrational periods for different values of anharmonicity. Using time interval 0–150 fs, where the VWP in the TI case [Fig. 8(a)] for all considered PECs show a high degree of localization, we found  $T = 14.12 \pm 0.01$ ,  $14.48 \pm 0.01$ , and  $14.76 \pm 0.06\text{ fs}$  in 95% t-CI, for the harmonic PEC,  $x_e\omega_e \approx 16\text{ cm}^{-1}$ , and  $x_e\omega_e \approx 32\text{ cm}^{-1}$ , respectively [Fig. 8(a), see legends]. In the case of OPI and MPI [Fig. 8(b)] we obtained, respectively,  $T = 14.12 \pm 0.01$ ,  $14.58 \pm 0.02$ , and  $14.91 \pm 0.06\text{ fs}$ . Small deviation in the vibrational frequency (yet nearly fully inside the errors) between the results of Figs. 8(a) and 8(b) can be understood from the two reasons: (i) faster delocalization of the VWP in the OPI and MPI case; (ii) slight change of the VWP shape in  $R$ - $t$  space [see Fig. 3(a)], when it approaches the delocalization time-region. Let us pay your attention, that the vibrational period increases with increase of the PEC anharmonicity. This behavior is in a full qualitative agreement to the analytical equation for the Morse potential oscillation period (B3), see Appendix B. Indeed, as one can see from Fig. 7, increase of the anharmonicity makes the PEC more shallow, so that the energy at the vertical transition  $U_v$  becomes smaller and  $T$  increases (B3).

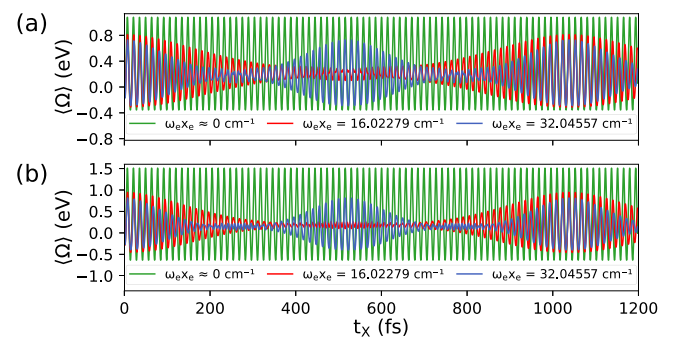


FIG. 8. TRXAS center of gravity trajectories (18) for different Morse potentials presented in Fig. 7 (see legends).  $T_{\text{rev}} = \infty$ , 1045 fs, and 523 fs for the TRXAS profiles correspondent to the  $\omega_e x_e = 0$ ,  $\omega_e x_e \approx 16.02\text{ cm}^{-1}$ , and  $\omega_e x_e \approx 32.05\text{ cm}^{-1}$ , respectively.  $\tau_X = 0.2\text{ fs}$ ,  $k = 1$ . (a) TI, (b) OPI and MPI.

Now we are in stage to define another important parameter of the ionic PEC, namely equilibrium internuclear distance. Using simple analytical derivation (see Appendix B) one can show that

$$R_i = R_g + \sqrt{\frac{T_{\text{rev}}}{2\mu\pi}} \ln[1 - \sqrt{1 - (T_0/T)^2}], \quad (19)$$

where  $R_g$  and  $R_i$  are equilibrium distances of the ground and ionic states, respectively, and  $T_0$  is period correspondent to the harmonic vibrational frequency. Let us note, that the fundamental (harmonic) frequency  $\omega_e$  for the ground ionic state can be accurately found using, for example, IR spectroscopy. In that case, using the values for  $T_{\text{rev}}$  and  $T$ , obtained above for the two anharmonic PECs of Fig. 7, one can easily compute the equilibrium ionic distance  $R_i$  using Eq. (19). In the case of TI we get the same value  $R_i \approx 2.01$  a.u. for both anharmonic PECs, which is close to the actual value of the 2.02 a.u. used in our simulations. In the case of OPI and MPI, when the  $R$  dependence of the ionization cross section is absent we get  $R_i \approx 1.99$  a.u. The small discrepancy in the definition of the  $R_i$  (1%–2%) can be explained by errors in definition of the vibrational and revival periods, resulting from deviation of the VWP shape closer to the time region of delocalization, as well as due to limited resolution in the TRXAS spectra. However, this example of a numerical experiment illustrates clearly practical approach how such important parameter as equilibrium distance of the ionic state can be found directly from TRXAS revival measurements with reasonable accuracy.

#### D. TRXAS revivals unveil subtle variations in potential energy curves

Let us now focus on a practical example, showing advantages of TRXAS scheme for detecting minor PEC deviation far from equilibrium. *Ab initio* methods provide PEC through computing system's electronic energy at different internuclear distances. Accuracy of the calculations varies for different quantum chemical methods, and, what is more important, it changes with increasing of the internuclear distance. As a general trend, the definition of molecular orbitals is less accurate far from the equilibrium resulting in less accurate energy values at larger  $R$ . Due to this, one can expect significant deviation in PEC computed with different methods and thus experimental PEC mapping is of great importance. Moreover, the experimental PEC for small system can be used as a benchmark for checking accuracy of quantum chemical methods.

Figure 9 shows *ab initio* PEC of the ground state of  $\text{NO}^+$  ion computed with rather small  $R$  step. It is worthwhile to note, that the PEC in general deviates from the Morse shape and in accurate simulations one has to apply the spline over *ab initio* points, rather than fitting to the Morse potential. In the figure we compare the spline performed with varied accuracy restricted by a number of decimal digits of computed energy (in Hartry) taken into account. The lower accuracy results in a small deviation of the potential at  $R > 2.15$  a.u. That small discrepancy between the PECs, however, induces an extreme change of the TRXAS trajectory, shown in Fig. 10. Indeed, the small change of the spline accuracy from  $10^{-3}$  to  $4^{-4}$  a.u. results in a sharp changes in the TRXAS. This is a

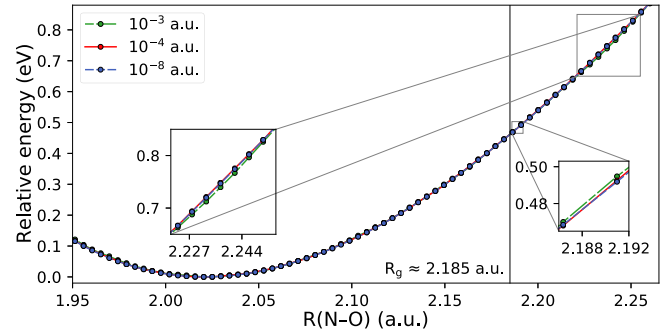


FIG. 9. *Ab initio* PEC for the cationic ground state approximated by spline with accuracy of  $10^{-3}$  (dash-dotted green line),  $10^{-4}$  (solid red line), and  $10^{-8}$  (dashed blue line) a.u. A small deviation is observed for  $R > 2.15$  a.u. The ground-state equilibrium  $R = 2.185$  a.u. is shown by the vertical line.

good illustration of the TRXAS sensitivity to the PEC shape, making it a powerful tool for PEC mapping. One can see, that further increase of the spline accuracy up to  $10^{-8}$  does not affect sufficiently the VWP trajectory (compare solid red and dashed blue lines in Fig. 10). For the high accuracy ( $10^{-4}$  and  $10^{-8}$ ) PEC the observation of the revival periods allows us to extract the anharmonicity, as it was discussed above. However, for the lower accuracy ( $10^{-3}$ ) a rather complex TRXAS trajectory is observed with no clear revival period, which suggests presence of higher anharmonicity terms.

It is instructive to compare TRXAS method for PEC parameters extraction with what can be done using a conventional photoelectron emission spectroscopy (PES). Theoretical simulations of PES spectra using the PECs presented in Fig. 7 are shown in Fig. 11. The spectra were convoluted with Gaussian of HWHM 0.01 eV in order to mimic a typical experimental broadening. The  $R$  dependence of the ionization cross section is taken into account for the PES spectra in Fig. 11(a), while the calculations in Fig. 11(b) use the  $R$ -independent cross section. The results illustrate that such a significant change of the PEC can be also distinguished in PES with small shifts of vibrational resonances, which requires rather high energy resolution, especially in the case of Fig. 11(a). However, the minor deviation between the PECs presented in Fig. 9 has no visible effect on the PES profiles (see Fig. 12). This is in a drastic contrast with TRXAS

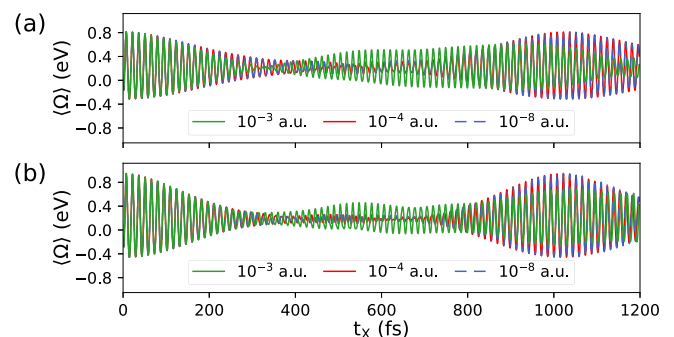


FIG. 10. TRXAS for the VWP dynamics computed with PECs from Fig. 9: (a) TI, (b) OPI and MPI.  $\tau_X = 0.2$  fs,  $k = 1$ .

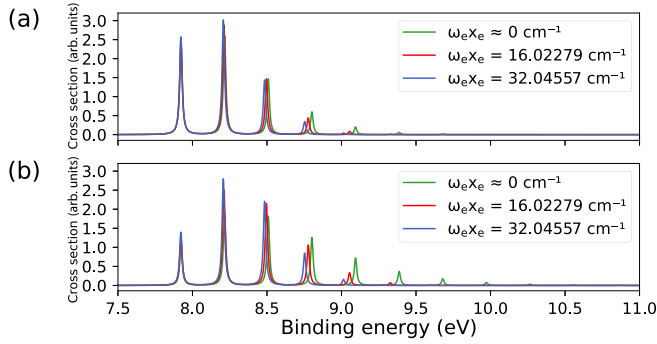


FIG. 11. Theoretical PES for PECs with different anharmonicity values (Fig. 7). (a)  $R$ -dependent and (b)  $R$ -independent ionization cross section; spectral broadening 0.01 eV (HWHM).

measurements of VWP revivals showing extreme trajectory changes for a small PEC deviation [Fig. 10].

#### IV. CONCLUSIONS

We developed an accurate theoretical framework for pump-probe scheme, where photoionization of a molecule with a short pulse triggers vibrational wave packets' and the absorption spectra of a time-delayed x-ray pulse allows us to probe the induced nuclear dynamics. Considering a fixed-in-space NO molecule as a showcase, we discuss the difference in the vibrational wave packet induced in the course of tunneling ionization with a strong IR pulse as compared with multiphoton IR ionization and one-photon UV ionization. Our numerical simulations of the pump-probe scheme were performed using fully quantum-mechanical description of the vibrational dynamics and time-dependent x-ray absorption profile.

Our simulations for various x-ray pulse durations (0.2–2.0 fs) and temporal envelope (Gaussian and quasirectangular) confirmed that the TRXAS profile reflects reasonably well the vibrational wave packets' trajectory, which makes this pump-probe technique a very useful tool for extracting parameters of molecular potential energy curves (anharmonicity and equilibrium bond length) with a high accuracy. Our numerical simulations for a number of variations of the original *ab initio* potential have shown the high sensitivity of TRXAS trajectory, even in the case of a subtle potential deviation

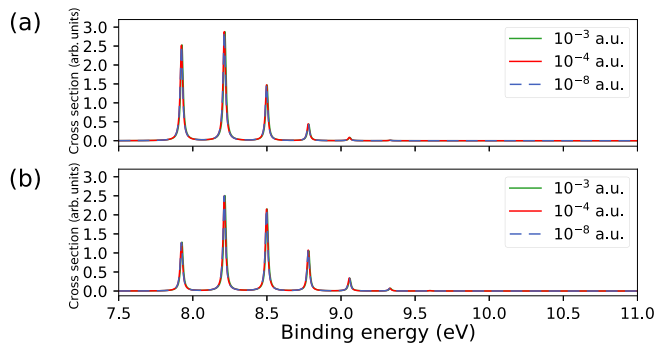


FIG. 12. Same PES calculations as in Fig. 11 but with PECs from Fig. 9.

not detectable by means of conventional photoemission spectroscopy. We also discussed a possibility to fully reconstruct vibrational wave packet in time and coordinate space from the TRXAS map. In the case of the ultrafast beating of the vibrational wave packet a proper balance between temporal and spectral resolution has to be found. The required pulse duration and coherence are available at the present day self-seeded XFELs and HHG x-ray light sources, giving a positive perspective for experimental mapping of the nuclear wave packet in real time and coordinate space. The method can be also adapted for SASE pulses making use of the covariance techniques. The pump-probe method studied is not limited to the ionic ground state discussed in the present paper but can be extended for valence neutral and ionic excited states of polyatomic molecules when other pump mechanisms are applied (e.g., two-photon absorption, optical Raman, etc.).

#### ACKNOWLEDGMENT

The reported study was funded by Russian Foundation for Basic Research (RFBR), Project No. 19-29-12015. The authors are thankful to Jiro Itatani, Nariyuki Saito, and Freddy Fernandes Guimarães for useful discussions.

#### APPENDIX A: $R$ AND INTENSITY DEPENDENCE OF THE TUNNELING IONIZATION RATE

Calculation for  $R$ -dependent ionization rate for the case of TI were performed for several values of the IR field strength and summarized in Fig. 13. One can see the critical dependence of the gradient on the field strength in the range of internuclear distances discussed in the paper.

#### APPENDIX B: MORSE POTENTIAL PARAMETERS

The Morse potential for an isolated electronic state can be written as

$$U(R) = D(1 - e^{-\alpha(R-R_0)})^2, \quad (\text{B1})$$

where  $D = \omega_e^2/4x_e\omega_e$  is the dissociation limit,  $\alpha = \sqrt{2\mu x_e\omega_e}$ ,  $\mu$  is reduced mass,  $R_0$  is the equilibrium internuclear distance,  $\omega_e$  is the harmonic frequency, and  $x_e\omega_e$  is the anharmonicity. It can be shown [56] that the period of vibrations for an

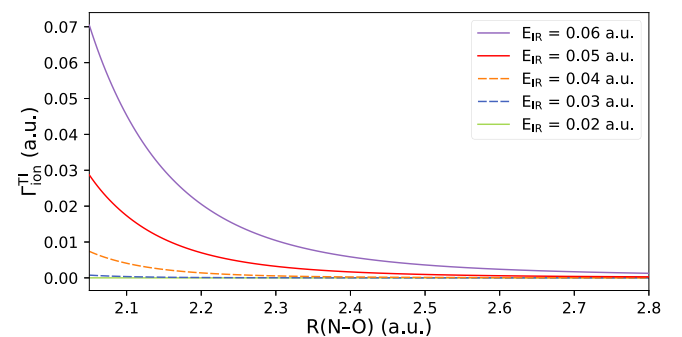


FIG. 13.  $\Gamma_{\text{ion}}^{\text{TI}}(R)$ , computed for several values of the IR electric field strength, see (9).

anharmonic oscillator can be found as

$$T(U_v) = \sqrt{2\mu} \int_{R_-}^{R_+} \frac{dR}{\sqrt{U_v - U(R)}}, \quad (\text{B2})$$

where  $R_{\pm}$  are the classical turning points at energy  $U_v$ , so that  $U(R_{\pm}) = U_v$ . Substitution of (B1) in (B2) and integration results in the following expression:

$$T(U_v) = T_0/\sqrt{1 - U_v/D}, \quad (\text{B3})$$

where  $T_0 = 2\pi/\omega_e$  is the period correspondent to the fundamental (harmonic) vibrational frequency.

In the ionization process considered here (Fig. 1), the right turning point  $R_+$  of the cationic ground state PEC  $U_i$  corresponds to the vertical transition of the ground state vibration wave function  $\psi_g$  localized near the equilibrium of the ground state  $R_g$ , so that  $U_v = U_i(R_{\pm}) = U_i(R_g)$ . Using that  $\alpha = \sqrt{2\mu\pi/T_{\text{rev}}}$ , one arrives at Eq. (19), which allows us to define the equilibrium position of the ionic potential  $R_i$  via the vibrational and revival times obtained from the TRXAS experiment.

- 
- [1] A. H. Zewail, Femtochemistry: Atomic-scale dynamics of the chemical bond, *J. Phys. Chem. A* **104**, 5660 (2000).
- [2] M. Kowalewski, B. P. Fingerhut, K. E. Dorfman, K. Bennett, and S. Mukamel, Simulating coherent multidimensional spectroscopy of nonadiabatic molecular processes: From the infrared to the x-ray regime, *Chem. Rev.* **117**, 12165 (2017).
- [3] F. Gel'mukhanov, M. Odelius, S. P. Polyutov, A. Föhlisch, and V. Kimberg, Dynamics of resonant x-ray and auger scattering, *Rev. Mod. Phys.* **93**, 035001 (2021).
- [4] J. Duris, S. Li, T. Driver, E. G. Champenois, J. P. MacArthur, A. A. Lutman, Z. Zhang, P. Rosenberger, J. W. Aldrich, R. Coffee, G. Coslovich, F. J. Decker, J. M. Glowina, G. Hartmann, W. Helml, A. Kamalov, J. Knurr, J. Krzywinski, M. F. Lin, J. P. Marangos *et al.*, Tunable isolated attosecond X-ray pulses with gigawatt peak power from a free-electron laser, *Nat. Photon.* **14**, 30 (2020).
- [5] A. S. Johnson, D. R. Austin, D. A. Wood, C. Brahm, A. Gregory, K. B. Holzner, S. Jarosch, E. W. Larsen, S. Parker, C. S. Strüber, P. Ye, J. W. Tisch, and J. P. Marangos, High-flux soft x-ray harmonic generation from ionization-shaped few-cycle laser pulses, *Sci. Adv.* **4**, (2018).
- [6] E. Lindroth, F. Calegari, L. Young, M. Harmand, N. Dudovich, N. Berrah, and O. Smirnova, Challenges and opportunities in attosecond and XFEL science, *Nat. Rev. Phys.* **1**, 107 (2019).
- [7] L. Varvarezos, J. Delgado-Guerrero, M. Di Fraia, T. J. Kelly, A. Palacios, C. Callegari, A. L. Cavalieri, R. Coffee, M. Danailov, P. Decleva, A. Demidovich, L. DiMauro, S. Düsterer, L. Giannessi, W. Helml, M. Ilchen, R. Kienberger, T. Mazza, M. Meyer, R. Moshhammer *et al.*, Controlling fragmentation of the acetylene cation in the vacuum ultraviolet via transient molecular alignment, *J. Phys. Chem. Lett.* **14**, 24 (2023).
- [8] S. Mukamel, Multidimensional femtosecond correlation spectroscopies of electronic and vibrational excitations, *Annu. Rev. Phys. Chem.* **51**, 691 (2000).
- [9] C. Miron, C. Nicolas, O. Travnikova, P. Morin, Y. Sun, F. Gel'mukhanov, N. Kosugi, and Victor Kimberg, Imaging molecular potentials using ultrahigh-resolution resonant photoemission, *Nat. Phys.* **8**, 135 (2012).
- [10] V. Kimberg and C. Miron, Molecular potentials and wave function mapping by high-resolution electron spectroscopy and *ab initio* calculations, *J. Electron Spectrosc. Relat. Phenom.* **195**, 301 (2014).
- [11] P. Hamm and M. Zanni, *Concepts and Methods of 2D Infrared Spectroscopy* (Cambridge University Press, 2011).
- [12] C. R. Baiz, B. Błasiak, J. Bredenbeck, M. Cho, J.-H. Choi, S. A. Corcelli, A. G. Dijkstra, C.-J. Feng, S. Garrett-Roe, N.-H. Ge, M. W. D. Hanson-Heine, J. D. Hirst, T. L. C. Jansen, K. Kwac, K. J. Kubarych, C. H. Londergan, H. Maekawa, M. Reppert, S. Saito, S. Roy *et al.*, Vibrational spectroscopic map, vibrational spectroscopy, and intermolecular interaction, *Chem. Rev.* **120**, 7152 (2020).
- [13] F. F. Guimarães, V. Kimberg, V. C. Felicíssimo, F. Gel'mukhanov, A. Cesar, and H. Ågren, Infrared-x-ray pump-probe spectroscopy of the NO molecule, *Phys. Rev. A* **72**, 012714 (2005).
- [14] F. F. Guimarães, Ph.D. thesis, Royal Institute of Technology, Stockholm, 2006 (unpublished).
- [15] V. C. Felicíssimo, F. F. Guimarães, F. Gel'mukhanov, A. Cesar, and H. Ågren, The principles of infrared-x-ray pump-probe spectroscopy. Applications on proton transfer in core-ionized water dimers, *J. Chem. Phys.* **122**, 094319 (2005).
- [16] N. Saito, H. Sannohe, N. Ishii, T. Kanai, N. Kosugi, Y. Wu, A. Chew, S. Han, Z. Chang, and J. Itatani, Real-time observation of electronic, vibrational, and rotational dynamics in nitric oxide with attosecond soft x-ray pulses at 400 eV, *Optica* **6**, 1542 (2019).
- [17] F. F. Guimarães, F. Gel'mukhanov, A. Cesar, and H. Ågren, Quantum wave packet revivals in IR + x-ray pump-probe spectroscopy, *Chem. Phys. Lett.* **405**, 398 (2005).
- [18] F. Neese, Software update: The ORCA program system, version 4.0, *Wiley Interdiscip. Rev. Comput. Mol. Sci.* **8**, e1327 (2018).
- [19] F. Neese, F. Wennmohs, U. Becker, and C. Riplinger, The ORCA quantum chemistry program package, *J. Chem. Phys.* **152**, 224108 (2020).
- [20] W. A. de Jong, R. J. Harrison, and D. A. Dixon, Parallel Douglas-Kroll energy and gradients in NWChem: Estimating scalar relativistic effects using Douglas-Kroll contracted basis sets, *J. Chem. Phys.* **114**, 48 (2001).
- [21] K. Eichkorn, O. Treutler, H. Öhm, M. Häser, and R. Ahlrichs, Auxiliary basis sets to approximate Coulomb potentials, *Chem. Phys. Lett.* **240**, 283 (1995).
- [22] E. J. Baerends, D. E. Ellis, and P. Ros, Self-consistent molecular Hartree-Fock-slater calculations I. The computational procedure, *Chem. Phys.* **2**, 41 (1973).
- [23] K. Eichkorn, F. Weigend, O. Treutler, and R. Ahlrichs, Auxiliary basis sets for main row atoms and transition metals and their use to approximate Coulomb potentials, *Theor. Chem. Acta* **97**, 119 (1997).

- [24] B. I. Dunlap, J. W. D. Connolly, and J. R. Sabin, On some approximations in applications of  $X\alpha$  theory, *J. Chem. Phys.* **71**, 3396 (1979).
- [25] C. Van Alsenoy, *Ab initio* calculations on large molecules: The multiplicative integral approximation, *J. Comput. Chem.* **9**, 620 (1988).
- [26] R. A. Kendall and H. A. Früchtl, The impact of the resolution of the identity approximate integral method on modern *ab initio* algorithm development, *Theor. Chem. Acta* **97**, 158 (1997).
- [27] J. Brown, A. Cole, and F. Honey, Magnetic dipole transitions in the far infra-red spectrum of nitric oxide, *Mol. Phys.* **23**, 287 (1972).
- [28] A. Stair Jr. and H. Gauvin, Research on optical infrared characteristics of aurora and airglow (artificial and natural), Aurora and Airglow, in *Proceedings of the NATO Advanced Study Institute, held 15–26 August, 1966 at the University of Keele, Staffordshire, England*, edited by Billy M. McCormac (Reinhold Publishing Co., New York, 1967), p. 365.
- [29] L. V. Keldysh, Ionization in the field of a strong electromagnetic wave, *Sov. Phys. JETP* **20**, 1307 (1965).
- [30] S. Blinov *et al.* (to be published).
- [31] J.-C. Liu, N. Ignatova, V. Kimberg, P. Krasnov, A. Föhlich, M. Simon, and F. Gel'mukhanov, Time-resolved study of recoil-induced rotation by x-ray pump–x-ray probe spectroscopy, *Phys. Chem. Chem. Phys.* **24**, 6627 (2022).
- [32] J.-C. Liu, J. Wang, N. Ignatova, P. Krasnov, F. Gel'mukhanov, and V. Kimberg, Role of the Cohen-Fano interference in recoil-induced rotation, *J. Chem. Phys.* **158**, 114304 (2023).
- [33] P. Lambropoulos, Topics on multiphoton processes in atoms, *Adv. At. Mol. Phys.* **12**, 87 (1976).
- [34] M. V. Ammosov, N. B. Delone, and V. P. Krainov, Tunnel ionization of complex atoms and of atomic ions in an alternating electromagnetic field, *Zh. Eksp. Teor. Fiz.* **91**, 2008 (1986) [*Sov. Phys. JETP* **64**, 1191 (1986)].
- [35] X. M. Tong, Z. X. Zhao, and C. D. Lin, Theory of molecular tunneling ionization, *Phys. Rev. A* **66**, 033402 (2002).
- [36] O. I. Tolstikhin, T. Morishita, and L. B. Madsen, Theory of tunneling ionization of molecules: Weak-field asymptotics including dipole effects, *Phys. Rev. A* **84**, 053423 (2011).
- [37] R. Saito, O. I. Tolstikhin, L. B. Madsen, and T. Morishita, Structure factors for tunneling ionization rates of diatomic molecules, *At. Data Nucl. Data Tables* **103–104**, 4 (2015).
- [38] T. Endo, A. Matsuda, M. Fushitani, T. Yasuike, O. I. Tolstikhin, T. Morishita, and A. Hishikawa, Imaging Electronic Excitation of NO by Ultrafast Laser Tunneling Ionization, *Phys. Rev. Lett.* **116**, 163002 (2016).
- [39] X. Urbain, B. Fabre, E. M. Staicu-Casagrande, N. De Ruet, V. M. Andrianarijaona, J. Jureta, J. H. Posthumus, A. Saenz, E. Baldit, and C. Cornaggia, Intense-Laser-Field Ionization of Molecular Hydrogen in the Tunneling Regime and Its Effect on the Vibrational Excitation of  $H_2^+$ , *Phys. Rev. Lett.* **92**, 163004 (2004).
- [40] A. Saenz, On the influence of vibrational motion on strong-field ionization rates in molecules, *J. Phys. B: At., Mol. Opt. Phys.* **33**, 4365 (2000).
- [41] N. Saito, Ph.D. thesis, The University of Tokyo, 2019 (unpublished).
- [42] M. Sabbar, H. Timmers, Y.-J. Chen, A. K. Pymer, Z.-H. Loh, S. G. Sayres, S. Pabst, R. Santra, and S. R. Leone, State-resolved attosecond reversible and irreversible dynamics in strong optical fields, *Nat. Phys.* **13**, 472 (2017).
- [43] F. Gel'mukhanov and H. Ågren, Resonant x-ray Raman scattering, *Phys. Rep.* **312**, 87 (1999).
- [44] R. Fink, A theoretical simulation of the  $1s \rightarrow 2\pi$  excitation and deexcitation spectra of the NO molecule, *J. Chem. Phys.* **106**, 4038 (1997).
- [45] P. Salek, F. Gel'mukhanov, and H. Ågren, Wave-packet dynamics of resonant x-ray Raman scattering: Excitation near the Cl  $L_{II,III}$  edge of HCl, *Phys. Rev. A* **59**, 1147 (1999).
- [46] P. Salek, A wave-packet technique to simulate resonant x-ray scattering cross sections, *Comput. Phys. Commun.* **150**, 85 (2003).
- [47] R. Schinke, *Photodissociation Dynamics. Spectroscopy and Fragmentation of Small Polyatomic Molecules* (Cambridge University Press, Cambridge, 1993).
- [48] V. Kimberg, A. Lindblad, J. Söderström, O. Travnikova, C. Nicolas, Y. P. Sun, F. Gel'mukhanov, N. Kosugi, and C. Miron, Single-Molecule X-Ray Interferometry: Controlling Coupled Electron-Nuclear Quantum Dynamics and Imaging Molecular Potentials by Ultrahigh-Resolution Resonant Photoemission and *ab initio* Calculations, *Phys. Rev. X* **3**, 011017 (2013).
- [49] N. Ignatova, V. V. da Cruz, R. C. Couto, E. Ertan, M. Odellius, H. Ågren, F. F. Guimarães, A. Zimin, S. P. Polyutov, F. Gel'mukhanov, and V. Kimberg, Infrared-pump-x-ray-probe spectroscopy of vibrationally excited molecules, *Phys. Rev. A* **95**, 042502 (2017).
- [50] P. K. Maroju, C. Grazioli, M. D. Fraia, M. Moiola, D. Ertel, H. Ahmadi, O. Plekan, P. Finetti, E. Allaria, L. Giannessi, G. D. Ninno, C. Spezzani, G. Penco, S. Spampinati, A. Demidovich, M. B. Danailov, R. Borghes, G. Kourousias, C. Eduardo, S. Dos *et al.*, Attosecond pulse shaping using a seeded free-electron laser, *Nature (London)* **578**, 386 (2020).
- [51] V. Kimberg and N. Rohringer, Stochastic stimulated electronic x-ray Raman spectroscopy, *Struct. Dyn.* **3**, 034101 (2016).
- [52] K. P. Huber and G. Herzberg, Constants of diatomic molecules, *Molecular Spectra and Molecular Structure: IV. Constants of Diatomic Molecules* (Springer US, Boston, 1979), pp. 8–689.
- [53] T.-C. Lim, Modification of morse potential in conventional force fields for applying FPDP parameters, *J. Math. Chem.* **47**, 984 (2010).
- [54] S. Schreck, A. Pietzsch, K. Kunnus, B. Kennedy, W. Quevedo, P. S. Miedema, P. Wernet, and A. Föhlich, Dynamics of the OH group and the electronic structure of liquid alcohols, *Struct. Dyn.* **1**, 054901 (2014).
- [55] V. Vaz da Cruz, F. Gel'mukhanov, S. Eckert, M. Iannuzzi, E. Ertan, A. Pietzsch, R. C. Couto, J. Niskanen, M. Fondell, M. Dantz, T. Schmitt, X. Lu, D. McNally, R. M. Jay, V. Kimberg, A. Föhlich, and M. Odellius, Probing hydrogen bond strength in liquid water by resonant inelastic x-ray scattering, *Nat. Commun.* **10**, 1013 (2019).
- [56] P. Amore, F. M. Fernández, and F. Fernández, Exact and approximate expressions for the period of anharmonic oscillators, *Eur. J. Phys.* **26**, 589 (2005).